Distributions of pore sizes and atomic densities in binary mixtures revealed by molecular dynamics simulations

Maxim A. Makeev[1] and Nikolai V. Priezjev[2]

[1]*Department of Chemistry, University of Missouri–Columbia, Columbia, Missouri 65211, USA*
[2]*Department of Mechanical and Materials Engineering, Wright State University, Dayton, Ohio 45435, USA*

We report on the results of a molecular dynamics simulation study of porous glassy media, formed in the process of isochoric rapid quenching from a high-temperature liquid state. The transition to a porous solid occurs due to the concurrent processes of phase separation and material solidification. The study is focused on topographies of the model porous structures and their dependence on temperature and average density. To quantify the pore-size distributions, we put forth a scaling relation that provides a satisfactory data collapse in systems with high porosity. We also find that the local density of the solid domains in the porous structures is broadly distributed, and, with increasing average density, a distinct peak in the local density distribution is displaced toward higher values.

I. INTRODUCTION

Physical processes taking place in a metastable liquid and solid matter have long been a focus of active research [1,2]. Among other phenomena, the bubble nucleation in metastable liquids has been under intense scrutiny due to both richness of the fundamental science and technological significance. The cavity (bubble) formation is known to occur in superheated liquids, at temperatures in excess of those of the boiling threshold, or in liquids under tension, at tensile pressures lower than the temperature-dependent saturation value of the pressure. An important milestone in the theory of bubble nucleation was set by Zel'dovich in 1942 [3]. Specifically, in Ref. [3], a one-dimensional theory of bubble nucleation in a liquid at high negative pressures was developed. Subsequent works have improved our understanding of the underlying physical and chemical processes at both macroscopic and microscopic levels [1,2]. Thus, it is established by now that the maximum tensile stress corresponds to the state in which the liquid becomes unstable with respect to an arbitrarily small disturbance of a mechanical or thermal nature [4]. The relaxation of a metastable state into a thermodynamically stable state occurs via a formation of a nucleus of a new phase. A statistical theory of relaxation of metastable states was developed by Patashinskii and Shumilo [5]. In the few last decades, a number of experimental and theoretical studies have been focused on the physical processes in both superheated and supercooled liquids, including those by Skripov and coworkers [6–9].

In Refs. [6–8], it was shown that the essential thermodynamic properties of liquids in the metastable states can be determined by experimental means. Later, the experimental data on the nucleation in superheated condensed noble gases (argon, krypton, and xenon) were summarized in Ref. [9] and compared to the theoretical results, obtained within the framework of the homogeneous nucleation theory [1,2]. A good agreement between theory and experiment was reported. The stability of coexisting phases in the liquid-vapor and crystal-liquid transitions was considered in Ref. [10]. It was found that, in the liquid-vapor transition, the stability of both phases on the equilibrium line decreases as temperature increases, while exactly the opposite trend is observed in the case of crystal-liquid transition. Important further advances in theoretical understanding are due to the use of statistical geometry in the theory of cavity nucleation. The statistical geometry of fluctuating void space (weak spot formation), which provided a microscopic basis for the theory of void nucleation in metastable matters, has been put forward in Refs [11,12]. More recently, a novel kinetic theory of homogeneous bubble nucleation was advanced, based upon the explicit calculation of the single-molecule evaporation and condensation rates as a function of the size of the vapor bubble [13].

In the past, the phenomenon of phase separation has also been studied in binary mixtures *via* both theoretical (Monte Carlo simulations) and experimental means. The following findings are worth noting. The mean-field theory approach [14] predicts that the initial instability in phase-separating systems is defined either by negative derivative of the chemical potential with respect to concentration in binary mixtures or by negative pressure derivative with respect to the local density in one-component fluids. In Ref. [15] the temporal evolution of pores in a glassy matrix was studied in model systems comprising liquid phase droplets of small volume fraction, immersed in the glassy phase. The authors reported on a novel mechanism of the dynamics of coarsening, which was found to be driven by migration and eventual coalescence of liquid droplets in the glassy phase.

More recently, the kinetics of the liquid-gas phase separation in a (80:20) binary Lennard-Jones mixture (Kob-Andersen model) was studied using molecular dynamics simulations in Refs. [16,17]. The phase separation was shown to occur during the dynamical evolution of the systems undergoing a rapid quenching. Among many other findings, these studies have provided important information on scaling relations, underlying the temporal evolution of phase-separating systems during a transition to a porous solid state, and reported on effects of the simulation system size

on the corresponding scaling behaviors. It should be noted that the Kob-Andersen (KA) binary mixture model [18], used in the aforementioned studies, is a well-known and successful atomistic model. In the past, the KA model has been used for a diverse range of applications, which include, but are not limited to, the simulation studies of Refs. [19–24]. The KA model has been proven useful for gaining insight into topics ranging from atomic-level structure of glasses to long-range dynamical correlations [25,26]. Also, it was instrumental in revealing the existence of spatio-temporal correlations in dynamical behavior of glassy materials (i.e., dynamic heterogeneity [26,27]). The KB model is used in this work to study the geometries of pores in phase-separated binary mixtures.

In the present study, the dynamical aspects of the phase-separation process are left beyond the scope. Rather, we fully concentrate on the topographical properties of the void space in the phase-separated systems and make an attempt to cover two extreme cases of void-space distributions, the ones that are characteristic for highly porous and dense glasses. Correspondingly, we consider systems where, at the upper bound, the void fraction is the largest one can achieve under the condition that the quenched samples are solid. At the lower bound, the void fraction is close to the one characteristic for conventional vitreous systems.

The remainder of the paper is organized as follows. The *modus operandi*, employed in this work, is described in the next section (Sec. II). In Sec. III we present our simulation results on the topography of porous structures and temperature dependence of the pore-size distributions. Also, we discuss the local density distributions in the solid domains of the phase-separated systems. Finally, in Sec. IV we summarize our principal findings and draw conclusions.

II. MODUS OPERANDI

In this work, the atomic systems are modeled as the KA binary (80:20) mixture of particles [18,28] in a periodic box. Within the KA model's framework, a pair of atoms $\alpha, \beta = \{A, B\}$ interact *via* the Lennard-Jones (LJ) potential of the form

$$V_{\alpha\beta}(r) = 4\,\varepsilon_{\alpha\beta}[(\sigma_{\alpha\beta}/r)^{12} - (\sigma_{\alpha\beta}/r)^6]. \qquad (1)$$

The parameters of the interatomic potential are set to $\varepsilon_{AA} = 1.0$, $\varepsilon_{AB} = 1.5$, $\varepsilon_{BB} = 0.5$, $\sigma_{AA} = 0.8$, $\sigma_{BB} = 0.88$, and $m_A = m_B$ [28]. The cutoff radius of the potential is fixed at $r_{c,\alpha\beta} = 2.5\,\sigma_{\alpha\beta}$. The units of length, mass, energy, and time are measured in $\sigma = \sigma_{AA}$, $m = m_A$, $\varepsilon = \varepsilon_{AA}$, and $\tau = \sigma\sqrt{m/\varepsilon}$, correspondingly. The equations of motion are integrated using the Verlet algorithm with the MD time step of $0.005\,\tau$ [29], and the temperature was controlled by velocity rescaling. Note that this work adopts the simulation methodology from Refs. [16,17] in what related to the dynamical evolution of the systems under consideration. Correspondingly, all the behavioral features pertained to the dynamics of solidification and the phase separation are equivalent to those reported on in the above references. The initial atomic configurations are prepared as follows. First, the systems of 3×10^5 atoms were thoroughly equilibrated at the temperature of $1.5\,\varepsilon/k_B$ during $3 \times 10^4\,\tau$ at a constant volume. Five independent samples were prepared at each density in the range $0.2 \leqslant \rho\sigma^3 \leqslant 1.0$. Thereby equilibrated systems were then quenched to low

temperatures; that is, well below the glass transition temperature of $0.435\,\varepsilon/k_B$ [16,17]. The temperature of the phase-separated systems was varied in the range from 0.02 to $0.20\,\varepsilon/k_B$, the increment being $0.01\,\varepsilon/k_B$. At each fixed temperature, the atomic systems were relaxed at a constant volume during the additional time interval of $10^4\,\tau$ to form porous structures. It was found that the final atomic configurations are stable and correspond to porous solids at different densities. Moreover, the mobility of atoms is suppressed; the atoms remain largely in their positions at the time scales accessible to molecular dynamics simulations. In Refs. [16,17], the authors found that the system-size effects become negligible when the number of atoms is no less than $\simeq 3 \times 10^5$. The choice of the system size used in this work is based upon this finding.

III. RESULTS

A. Notes on the process of void-space formation

As made explicit above, the transition to the phase-separated states at a constant volume occurs *via* concurrent decomposition of the systems into material and void domains, and solidification of the former. The processes take place during a rapid quenching to a low-temperature state from a liquid state. The underlying physical mechanisms, responsible for phase separation, are nucleation and spinodal decomposition. The study, however, does not include the temporal aspects, and therefore the nature of transition is omitted from further discussion. In Fig. 1 we show the representative examples of the topographical patterns, obtained in our simulations study. The major goal is to illustrate the larger-scale patterns in the solidified samples. Two main factors in shaping topography of the porous systems can be identified as the average density and temperature of phase-separated solids. It was found that the topographical patterns vary significantly with $\rho\sigma^3$. The void-space forms conglomerates of complex nanometer-sized pores. Formation of nanometer-scale channels running across the entire sample is also found to occur at low values of $\rho\sigma^3$. The channels possess distinctly different characteristic length scales, as compared to nanometer-scale (in all three dimensions) voids. Also noteworthy is the observation that, in the whole range of average density variation, the pores show no tendency to adopt even a quasispherical shape. This observation can be of essence for theoretical models dealing with nanoporous continua. The deviations from sphericity can be interpreted as resulting from highly inhomogeneous and asymmetric tension in the systems. As mentioned above, the degree of porosity in this work is varied in a rather wide range. This allows for comparison of the present results with findings reported in previous studies. While the low-density (high porosity) systems have not been investigated in sufficient detail to compare our theoretical predictions with experimental works, highly dense systems have been the focus of experimental studies, which makes a qualitative comparison feasible. Indeed, the simulation results of our study show that the void-size distribution at $\rho\sigma^3 = 0.9$ is that of a random quantity. This is consistent with the recent experimental results of Ref. [30], where it was shown that the quenched-in free volume in glasses is randomly distributed. Furthermore, the shape of the distribution at the above density is similar to
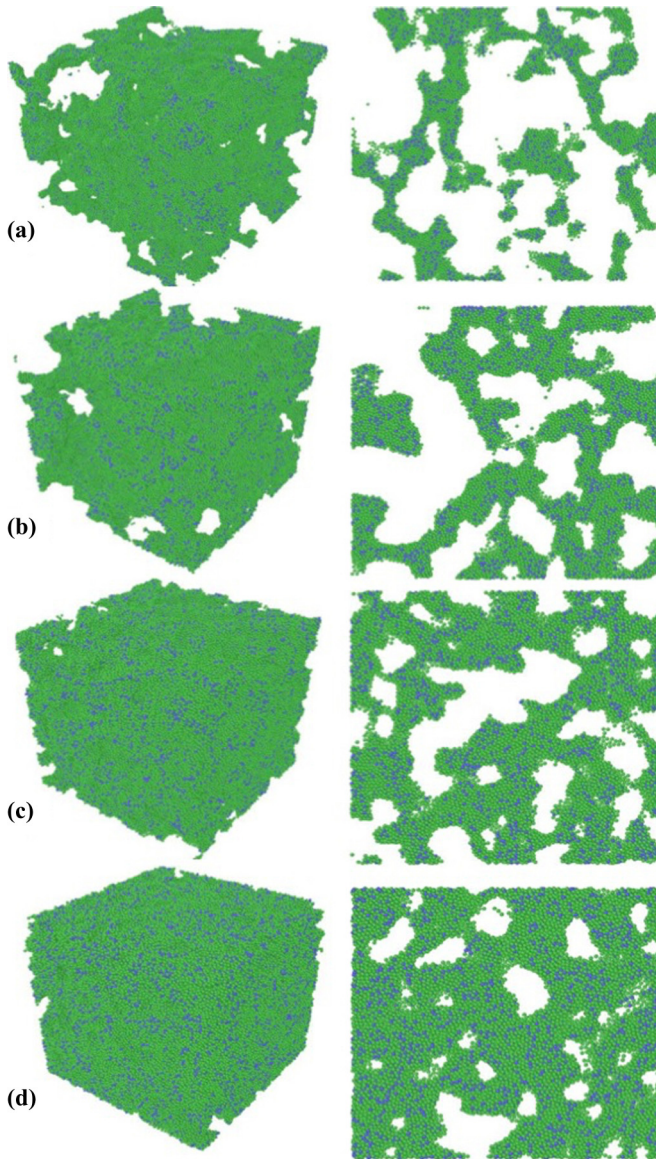
FIG. 1. Equilibrium instantaneous atomic configurations of the porous glass, computed at different values of $\rho\sigma^3$: (a) 0.3, (b) 0.5, (c) 0.7, and (d) 0.9 (from top to bottom). All the configurations are obtained at $T = 0.05\,\varepsilon/k_B$. The left panels show the full three-dimensional plots of the atomic configurations, and the right panels display slices of the central parts of the simulation cell with thickness of $5\,\sigma$. Different colors mark atomic types A and B.

FIG. 2. The average pressure, P, in equilibrium systems as a function of temperature, T, for the indicated values of $\rho\sigma^3$. The inset shows the scaling collapse using $P/T \sim \rho^\alpha$ relation. See text for details.

the experimental results, obtained for the hole-radius density distribution in polycarbonate and polystyrene [31]. As discussed below (see Fig. 3 and discussion), the differences in the pore-size distributions in the high- and low-porosity systems manifest themselves in different scaling behaviors. In particular, the data at $\rho\sigma^3 = 0.9$ (and higher values of $\rho\sigma^3$) do not obey the same scaling, as the one obtained for systems with high porosities.

As discussed above, the cavitation in liquids takes place due to overcritical negative tension, applied to the system. The systems under consideration are not under any external load. However, in our study, we also find that the transition
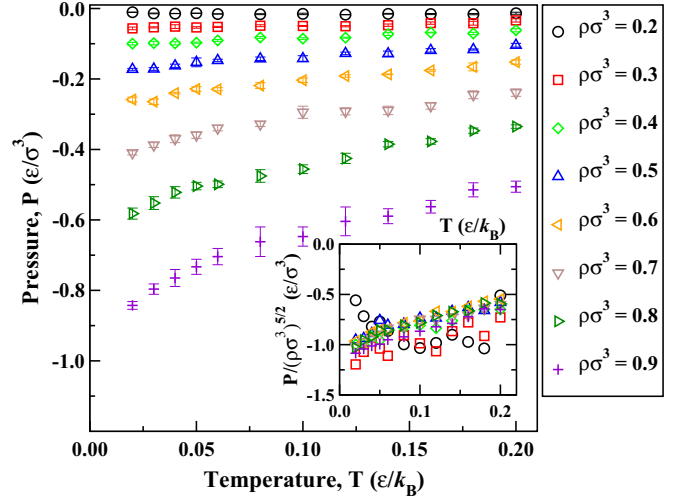
to the porous structure is driven by negative pressure. In the past, a number of studies were devoted to the mechanism of void formation under negative pressure. Thus, cavitation in LJ model systems was studied in Ref. [32] using the Monte Carlo method. It was found that there exists a critical density at which the volume fraction of void vanishes, and this density coincides with the minimum in the pressure versus density curve for inherent structures (the Sastry curve) at a negative pressure. In a subsequent study of Ref. [33], the Sastry curves were used to show that the properties of glass-forming mixtures depend on softness of the interatomic potentials. In this respect, it should be noted that our study employs the interaction potential with fixed softness. Given all the above, it is important to provide some insights into the details of pressure variation with temperature of the solid regions and as a function of $\rho\sigma^3$.

In Fig. 2, the mechanical pressure versus temperature dependencies are plotted for the model systems with different $\rho\sigma^3$. As follows from Fig. 2, the transition to solidified porous states and dynamical evolution of the systems take place under negative pressure, which relaxes in the process of phase separation. At very low densities (see $\rho\sigma^3 = 0.2$ in Fig. 2), the pressure is relatively small and its absolute value is an increasing function of temperature when $T \lesssim 0.1\,\varepsilon/k_B$. As temperature increases above $\simeq 0.1\,\varepsilon/k_B$, the pressure becomes a decreasing function of temperature.

The pressure variation as a function of temperature at densities $\rho\sigma^3 \geqslant 0.3$ is universal, and, depending on the temperature range, three different regimes can be identified. As is evident in Fig. 2, in this range of densities, the pressure increases monotonically with temperature. However, the rate of increase at temperatures below $\simeq 0.05\,\varepsilon/k_B$ differs considerably from those observed at intermediate temperatures and those close to $\simeq 0.20\,\varepsilon/k_B$. Thus, at temperatures higher than $\simeq 0.07\,\varepsilon/k_B$, the dependencies flatten out significantly. The decrease in negative pressure is due to two important factors. First, the microstructural rearrangements are fully controlled by thermally activated processes. However, the average density is the

factor which affects collective motion and, in effect, shapes the pore topography. An increase in density suppresses the mobility of atoms at a fixed temperature. Correspondingly, at low temperatures, the degree of structural relaxation depends strongly on temperature. In the intermediate range of temperatures, between $\simeq 0.05\,\varepsilon/k_B$ and $0.15\,\varepsilon/k_B$, the rates of pressure variation are smaller compared to the low-temperature range, yet a significant decrease in pressure magnitude is observed at all densities studied. At low densities, this regime corresponds to a nearly complete relaxation at any temperature (above $\simeq 0.15\,\varepsilon/k_B$). As expected, in the third region, a nearly flat dependence is observed. Note that *qualitative features* of the topographical patterns do not change with temperature. Also, in the whole range of temperatures, the observed variations in pressure with temperature are rather small, as compared to the effects due to the average density. Indeed, the pressure changes by approximately an order of magnitude, while the average density varies in the range $\rho\sigma^3 \in [0.2, 0.9]$.

In order to establish a more quantitative basis for estimating the effect of density, in the inset to Fig. 2 we show the data collapse obtained by using the scaling relation $P/T \sim \rho^\alpha$ with $\alpha \simeq 5/2$. Given such a strong dependence, we conclude that pressure is largely controlled by the *average density* in a wide range of $\rho\sigma^3$. Also, pressure depends on topological properties of void domains. One of the possible explanation for such a behavior is that it is associated with surface energy. However, further studies of the near-surface effects should be performed to uncover all the details of the observed behavior. Note that the deviations from the scaling behavior are quite significant at $\rho\sigma^3 \leq 0.3$ and $\rho\sigma^3 = 0.9$.

B. Pore size distribution functions

Further analysis involves pore-size, d_p, distribution (PSD) functions, $\Phi(d_p)$. To quantify the topographical properties of the ensembles of pores (see Fig. 1 for illustration), we employed the methods and the computer code developed in Refs. [34,35]. Figure 3 shows the behavior of the PSD functions, computed at different values of $\rho\sigma^3$. As can be observed in Fig. 3, in the region of small pore sizes, each PSD is an increasing function of d_p. This behavior holds for pore sizes below a characteristic value. Note that both the rate of increase of the PSDs and their magnitudes are smallest at $\rho\sigma^3 = 0.2$. In general, both of these quantities are increasing functions of $\rho\sigma^3$. At larger d_p values (than the characteristic one), the PSDs flatten out. One more common feature of systems with $\rho\sigma^3 < 0.9$ is that they exhibit a peak at d_p values close to maximum pore-sizes. The above behavior is qualitatively different from that of dense (low-porosity) systems. In this respect, the cases with $\rho\sigma^3 = 0.9$ and 1.0 serve as representative examples. Indeed, in dense systems, the PSDs profiles are close to Gaussian (see the orange dashed curve in Fig. 3). In this case, the PSDs are fully described by the position of the peak and the width of the distribution. Thus, one can approximately define the critical value of density, $\rho_c\sigma^3 = 0.9$, at which the transition from the porous system-type behavior to bulk-type behavior is observed. As discussed above, the bulk-type behavior is characterized by Gaussian distribution of pore sizes and distinctly differs from that characteristic for systems with high porosity.
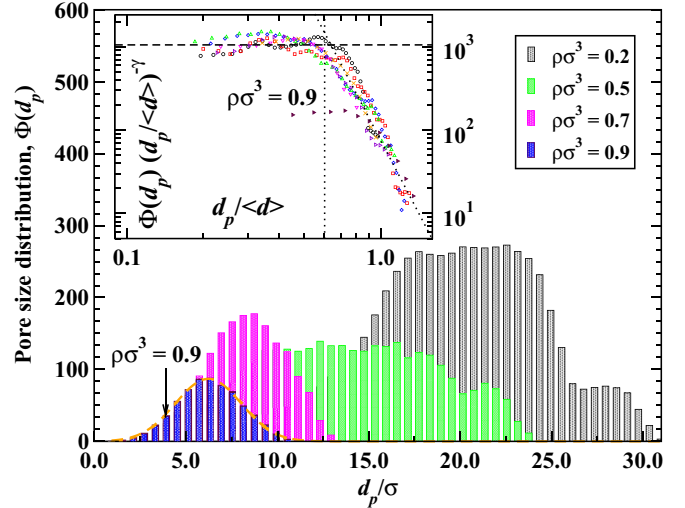

FIG. 3. The pore size distribution functions, $\Phi(d_p)$, computed for systems with densities $\rho\sigma^3 \in \{0.2, 0.5, 0.7, 0.9\}$ and $T = 0.05\,\varepsilon/k_B$. In the analysis, the original bin size is fixed at $\simeq 0.05\,\sigma$. Subsequent averaging was performed within $\simeq 0.5\,\sigma$; a reduced set of data points for each $\rho\sigma^3$ is shown for clarity. The dashed orange curve is a Gaussian fit to the $\rho\sigma^3 = 0.9$ data. The inset shows the data collapse for all densities according to Eq. (2). The same color code as in Fig. 2.

As shown below, there exists a universal scaling in the regime of small and intermediate length scales. To formulate the corresponding scaling law, let us introduce the average pore diameter as $\langle d \rangle = \sum_{i=1}^{M} d_{p(i)}^2 \, n_{d_{p(i)}} / \sum_{i=1}^{M} d_{p(i)} \, n_{d_{p(i)}}$, where $n_{d_{p(i)}}$ is the number of pores having a discrete diameter $d_{p(i)}$ and M is the number of the discretization points [36]. Further, for the equilibrium continuous PSDs, $\Phi(d_p)$, we postulate the following scaling ansatz:

$$\Phi(d_p) \sim (d_p/\langle d \rangle)^\gamma \, f(d_p/\langle d \rangle). \tag{2}$$

The function $f(x)$ possess the following properties: (a) $f(x \leqslant 1) \sim$ const and (b) $f(0.5 < x < 1.5) \sim x^{-\gamma}$. We applied the scaling form to the data obtained on all the considered herein systems. The scaling collapse for all $\rho\sigma^3$ is shown in the inset to Fig. 3. As can be observed in the figure, the data collapse is quite convincing. The following findings are noteworthy. First, there exists a universal exponent $\gamma \simeq 3$, which describes the data for all densities up to $\rho\sigma^3 = 0.8$ inclusive. Second, the average pore diameter is a strong function of porosity. By a numerical analysis of the corresponding quantities, we found the following relation between the average pore size and porosity: $\langle d \rangle \sim p^\delta$, where δ is close to 2/3, as shown in Fig. 3. In essence, this relation signifies the fact that the average pore size is determined by the average surface area of the void space inside the solid material. The maximum pore diameter, d_m, is defined by the effective size of the available free space, which can be approximated as $\lambda = p^{1/3} L$, where L is the linear system size. The relation holds for all densities, such that $\rho\sigma^3 \leqslant 0.8$. Also, the deviation from the scaling law, Eq. (2), occurs at the length scales close to d_m. This indicates the existence of two independent length scales in the system: $\langle d \rangle$ and d_m. The effects associated with the second length scale manifest themselves by the observed deviations in the scaling behavior at $d_p/\langle d \rangle$ values above ≈ 1.5 (see the inset in Fig. 3).
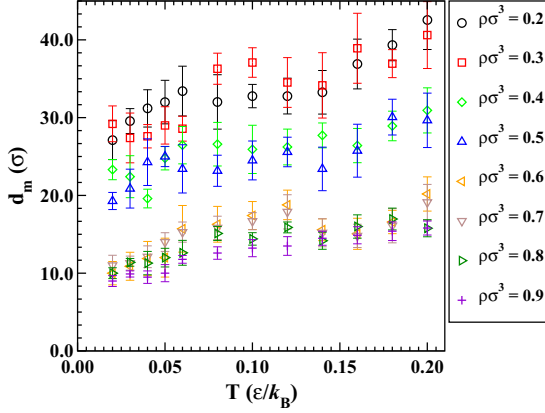
FIG. 4. The maximum pore diameter, d_m, is plotted as a function of temperature for the tabulated values of $\rho\sigma^3$.

FIG. 5. On-lattice local density distribution functions, $\langle\rho\rangle_R$, are shown for the normalized average density, $\rho\sigma^3$, values: (a) 0.2, (b) 0.3, (c) 0.4, (d) 0.5, (e) 0.6, (f) 0.7, (g) 0.8, (h) 0.9, and (i) 1.0. The distribution functions are computed using the bin size of $\langle\rho\rangle_R^{\max}/400$ and $T = 0.05\,\varepsilon/k_B$; no averaging of any kind is involved.

The behavior of the PSDs was studied in a temperature interval between $0.02\,\varepsilon/k_B$ and $0.20\,\varepsilon/k_B$. We found that the general shape of the PSD functions is preserved in the whole range of temperature variation. At small pore diameters, all the PSD functions follow a power-law behavior, with the power-law exponent close to $\simeq 3.0$. Further, in the range of intermediate d_p values, $\Phi(d_p)$ flattens out. The scaling relation, Eq. (2), holds in the whole temperature range studied. Correspondingly, a variation in temperature changes only the width and height of the PSDs, leaving the other features intact. Note, however, that, in proximity to the maximum pore diameter, d_m, a peak is observed. We found that the magnitude of the peak is nearly negligible, when temperature is less than $\simeq 0.05\,\varepsilon/k_B$. At higher temperatures the peak magnitude increases, being $\simeq 100\,\%$ greater than that of the plateau region at $T = 0.2\,\varepsilon/k_B$. As explained above, the PSD functions can be regarded as piecewise combinations of two distinctive parts. The first part corresponds to small and intermediate pore diameters and is described by Eq. (2). The second part corresponds to a separate peak in the vicinity of d_m. In this region, the scaling breaks down. Although, the general shape of the PSDs is not affected by the variation in temperature, the parameters of distributions vary substantially. The maximum pore diameter versus temperature is plotted in Fig. 4 at different values of $\rho\sigma^3$. As can be observed in the figure, at every $\rho\sigma^3$ value, d_m is an increasing function of temperature, as expected. Moreover, the relative maximum increments in d_m due to temperature variations are independent of $\rho\sigma^3$ and can roughly be estimated as $\simeq 30\,\%$. One curious feature of behavior is worth noting. Three density ranges can be discriminated in Fig. 4. In each density range, the curves show remarkably similar behavior not only in what related to d_m values, but also to the specifics of the functional dependence. From this behavior, one can infer that there exist dynamical constraints on the pore evolution, such that there is no continuous dependence of the pore-formation dynamics on density.

It might also be instructive to compare the present study with the predictions of Ising-type models of domain growth with conserved order parameter. With regard to dynamics of domain growth, it was shown that in three dimensions the domain size grows in time as $\sim t^{1/3}$ [37]. In the case of Model B (Ising model with the usual Kawasaki spin-exchange kinetics),
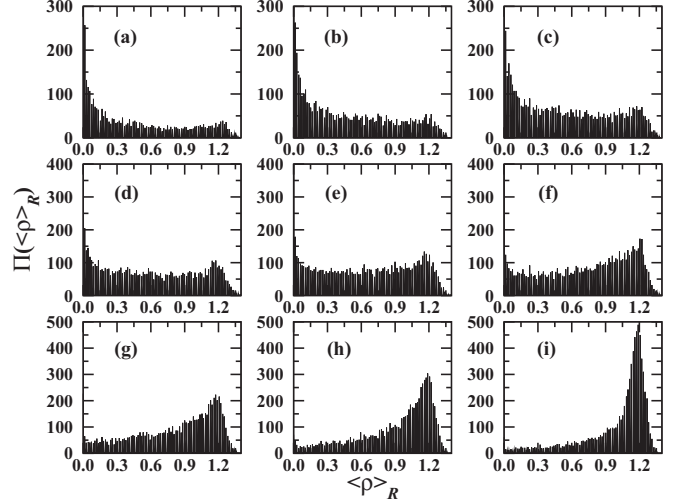
the same exponent has been observed in simulations studies, performed in two and three dimensions [38]. Note that similar power-law exponents have been derived in Refs. [16,17] for the systems under consideration. In the case of Model S [the usual Kawasaki spin-exchange kinetics (Model B) with a kinetic constraint], the domain size distribution function was obtained in Ref. [39]. At small and intermediate length scales, the scaling form is a power law, with the exponent equal to $-(1/2)$. At large domain sizes, it exhibits an exponential decay [39]. Further work is needed to understand the behavior of pore-size distributions in the phase separating systems and to establish their possible relation to domain-growth problems.

C. Local density distributions

In the preceding sections, we studied the properties of pores in the phase-separated systems. In what follows, the focus is put on the solid domains in the model systems under consideration. In particular, we compute local densities in the solid-state domains. Henceforth, the local density is defined by a number of atoms located within a predefined radial range centered on a site of the cubic lattice $L \subset \mathbb{R}^3$. Correspondingly, for each lattice site, we define a closed ball, $B_R = \{R \in \mathbb{R}^3 : \sum_{j=1}^{3} R_j^2 \leqslant R_0^2\}$, where $R_0 = |\vec{R}_0|$ is a fixed rational number. Then the average density is given by $\langle\rho\rangle = 1/V \sum_{i=1}^{N} \delta(\vec{r}_i) = N/V = \rho\sigma^3$. The on-site *local density* is computed as $\langle\rho\rangle_R = 1/B_R \int_{B_R} dR^3 \delta(\vec{r}_i - \vec{R})$, where the integral is taken over B_R. Note that $\langle\rho\rangle_R$ depends on R_0. In our calculations, we used a fixed value of $R_0 = 2.5\,\sigma$. The rationale for choosing this value is based upon the behavior of $\langle\rho\rangle_R(R_0)$ in dense (nearly void-free) systems. At this value of R_0, the local density becomes constant and thus is equal to the *average density* of a homogeneous nonporous system. That is why $\langle\rho\rangle_R$ can be regarded as *a measure of deviation of the local density from the average density* of homogeneous dense solid. In Fig. 5, we plot the local density distribution functions,

$\Pi(\langle\rho\rangle_R)$, computed at nine different average densities. As can be seen in the figure, depending on $\rho\sigma^3$, three different types of behavior can be discriminated (see lower, middle, and upper panels of the figure). In the regime of small $\rho\sigma^3$ values (upper panel), the major characteristic features are the following: (a) a strong peak in the vicinity of zero density and (b) $\Pi(\langle\rho\rangle_R)$ is a decreasing function of $\langle\rho\rangle_R$. This is not an unexpected behavior for phase-separating systems with a large fraction of pores. Indeed, pores and thin solid domains contribute to the peak at zero and small value of $\langle\rho\rangle_R$. Note that the surface-to-volume ratio in solid domains is rather large in this regime, and therefore particles located in near-surface regions contribute significantly to the behavior at intermediate $\langle\rho\rangle_R$. The functional dependence with $\langle\rho\rangle_R$ resembles closely a continuous decay. Note, however, that there is a peak in the region slightly above $\langle\rho\rangle_R = 1.2$. The nature of the peak is discussed below.

Lets us now turn the attention to the opposite case of a dense, nearly homogenous solid. The panels (g), (h), and (i) in Fig. 5 correspond to large $\rho\sigma^3$ values. The behavior is, in a sense, the opposite to the one, observed at small values of $\rho\sigma^3$. Indeed, the highest peak is expected to be at a value close to the average density of the solid material. The plateau centered at approximately $\rho\sigma^3 = 0.6$ is due to the near-surface regions of the solid domains, where the numbers of atoms is close to one half of the bulk value. Once again, a peak at a value of $\langle\rho\rangle_R$ close to 1.2 is observed. In the region of small values of $\langle\rho\rangle_R$, only a small deviation from zero can be seen. Those are due to local fluctuations in void fractions that can be regarded as microstructural defects. The peaks in the intermediate range of the local density are due to atoms located in near-surface regions of pores of small sizes. At the intermediate values of $\langle\rho\rangle_R$, the patterns can be regarded as a superposition of the two cases, discussed above. The solid domains are represented by the peaks at the densities characteristic for large values of $\rho\sigma^3$. The peaks near zero decrease in magnitude with the average density, while, at intermediate values of $\langle\rho\rangle_R$, the behavior is characteristic for phase-separating systems with a large surface-to-volume ratio.

The behavior of $\Pi(\langle\rho\rangle_R)$ functions in the regions close to the maximum density requires an additional analysis. Those regions correspond to the density of solid domains away from the interfaces with the pores, and thus are of interest for several reasons. First, mechanical response properties of porous materials depend on the density of the solid material in the system. Second, diffusivity (as mentioned above, it is highly suppressed in a solid state) is generally a decreasing function of density [40]. Here we focus on the behavior of the average density of solid domains as a function of porosity. To get a measure of the solid phase average density, we define the quantity denoted as $\langle\rho\rangle_S$, such that it provides an average over the density distributions in the region around the maximum corresponding to the solid fraction (in Fig. 5, the average solid fraction density corresponds to the peaks around $\langle\rho\rangle_R = 1.2$). To find the average, we assume that the peaks in regions close to $\langle\rho\rangle_R = 1.2$ can be approximated as Gaussian forms. Then the parameters of each Gaussian curve can be obtained from the corresponding numerical fits. The porosity, p, was computed using the methods and the computer code developed by the authors of Refs. [34,35]. In Fig. 6 we plot $\langle\rho\rangle_S$, as a function of p. As follows from the figure, the solid-fraction density of the porous systems does not
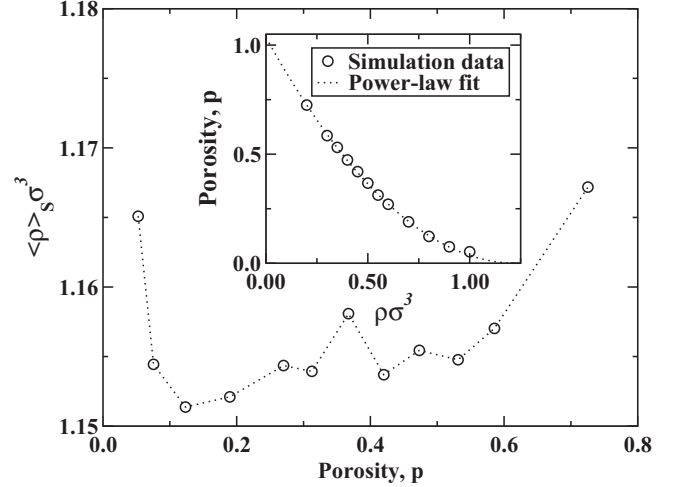

FIG. 6. Average density of solid domains, $\langle\rho\rangle_S$, is plotted as a function of the porosity, p. The inset shows the porosity versus $\rho\sigma^3$ dependence (open circles). The power-law fit to the simulation data is indicated by the dashed curve. The fitting procedure is discussed in the text.

differ much from that of the dense ones. In the wide porosity range studied, the maximum variation in the density is less than $\simeq 5\%$. The behavior of $\langle\rho\rangle_S$ with porosity, however, possesses some noteworthy features. First, there is a rather abrupt change in $\langle\rho\rangle_S$ in the region of small values of p. Second, in the high porosity limit, $p \geqslant 0.6$, the density is a strongly increasing function of p. At the intermediate values of p, $\langle\rho\rangle_S$ demonstrates a moderate growth. This range spans p values from $\simeq 0.1$ to $\simeq 0.5$. Next, we discuss the behavior of porosity with the average density, $\rho\sigma^3$. The result is shown in the inset to Fig. 6. As our analysis shows, the behavior can be represented by the following scaling relation $p \propto (\rho_c\sigma^3 - \rho\sigma^3)^\gamma$. In this formula, $\rho_c\sigma^3$ is the critical density, corresponding to $p = 0$. Curiously enough, the value obtained from the fitting is $\rho_c\sigma^3 = 1.24$. Note that the value $\rho_c\sigma^3 = 1.25$ was reported in Ref. [33] as the critical density below which LJ systems develop voids upon isochoric energy minimization. The computed power-law exponent is $\gamma \simeq 2.0$. The above relation works well at both the small and the intermediate values of $\rho\sigma^3$. At the values of $\rho\sigma^3$ greater than $\simeq 0.8$, deviations from the scaling behavior occur. Note that, in this region, $\langle\rho\rangle_R$ is a strongly increasing function of p. This means that the density changes drastically with a minor variation of p. The behavior is consistent with the large negative pressures in this range of $\rho\sigma^3$.

IV. CONCLUSIONS

In this paper, we studied the structural and thermodynamic properties of binary mixtures with varied porosity, obtained by an isochoric rapid quench from a liquid phase to low-temperature porous systems. The transition to porous vitreous state occurs as a result of instability, defined by negative thermodynamics derivatives of the chemical potential and pressure with respect to the concentration and the local density, respectively. The temperature of equilibrated porous systems was varied in a relatively wide range to reveal effects of temperature on the thermodynamical properties and structural specifics of the

porosity patterns. We computed the temperature dependence of pressure in the systems with different densities and deduced a scaling law governing the behavior of the pressure versus temperature dependence with average density. Further, the pore-size distribution functions were studied. We found that in the systems with porosity exceeding a characteristic value, the distribution function obeys a single scaling relation. For highly dense systems, the distribution resembles closely a Gaussian; this finding is in agreement with available experimental data. It was found that a change in temperature of porous systems does not alter general shape of the pore-size distribution functions, the major effect being a widening of the curves. The local density distribution functions for samples with varied average density were also scrutinized. We found that local density of the solid domains is a decreasing function of porosity in the high porosity limit, while it decreases with porosity for dense systems. The present study can be of use for design of porous absorbent materials and related technologies. Also, it can provide some information for the general area of porous materials.

ACKNOWLEDGMENTS

[1] V. P. Skripov, *Metastable Liquids* (Wiley, New York, 1973).

[2] P. G. Debenedetti, *Metastable Liquids: Concepts and Principles* (Princeton University Press, Princeton, NJ, 1996).

[3] Y. B. Zel'dovich, On the theory of new phase formation. Cavitation, Zh. Eksp. Teor. Fiz. **12**, 525 (1942).

[4] V. P. Skripov, Behavior of liquid thermodynamic stability under superheating and supercooling, J. Eng. Phys. **59**, 1135 (1990).

[5] A. Z. Patashinskii and B. I. Shumilo, Theory of relaxation of metastable states, Sov. Phys. JETP **50**, 712 (1979).

[6] V. G. Baidakov, V. P. Skripov, and A. M. Kaverin, Attainable overheating of liquid argon, Sov. Phys. JETP **38**, 557 (1974).

[7] V. G. Baidakov, V. P. Skripov, and A. M. Kaverin, Experimental study of liquid argon in the metastable state, Sov. Phys. JETP **40**, 335 (1975).

[8] V. G. Baidakov and V. P. Skripov, The velocity of sound and the thermodynamic stability of liquid argon, Sov. Phys. JETP **48**, 509 (1978).

[9] V. P. Skripov, V. G. Baidakov, and A. M Kaverin, Nucleation in superheated argon, krypton and xenon liquids, Physica A **95**, 169 (1979).

[10] V. P. Skripov and M. Z. Faizullin, Continuation of the melting curve and the spinodal of a stretched crystal and a liquid, Doklady Phys. **51**, 106 (2006).

[11] S. Sastry, P. G. Debenedetti, and F. H. Stillinger, Statistical geometry of particle packings. II. "Weak spots" in liquids, Phys. Rev. E **56**, 5533 (1997).

[12] A. Vishnyakov, P. G. Debenedetti, and A. V. Neimark, Statistical geometry of cavities in a metastable confined fluid, Phys. Rev. E **62**, 538 (2000).

[13] V. K. Shen and P. G. Debenedetti, A kinetic theory of homogeneous bubble nucleation, J. Chem. Phys. **118**, 768 (2003).

[14] D. Gunton, M. San Miguel, and P. S. Sahni, in *Phase Transitions and Critical Phenomena*, edited by C. Domb and J. L. Lebowitz, Vol. 8 (Academic, New York, 1983), p. 267.

[15] D. Sappelt and J. Jackle, Spinodal decomposition with formation of a glassy phase, Europhys. Lett. **37**, 13 (1997).

[16] V. Testard, L. Berthier, and W. Kob, Influence of the Glass Transition on the Liquid-Gas Spinodal Decomposition, Phys. Rev. Lett. **106**, 125702 (2011).

[17] V. Testard, L. Berthier, and W. Kob, Intermittent dynamics and logarithmic domain growth during the spinodal decomposition of a glass-forming liquid, J. Chem. Phys. **140**, 164502 (2014).

[18] W. Kob and H. C. Andersen, Scaling Behavior in the ß-Relaxation Regime of a Supercooled Lennard-Jones Mixture, Phys. Rev. Lett. **73**, 1376 (1994).

[19] L. Angelani, R. Di Leonardo, G. Ruocco, A. Scala, and F. Sciortino, Saddles in the Energy Landscape Probed by Supercooled Liquids, Phys. Rev. Lett. **85**, 5356 (2000).

[20] K. Broderix, K. K. Bhattacharya, A. Cavagna, A. Zippelius, and I. Giardina, Energy Landscape of a Lennard-Jones Liquid: Statistics of Stationary Points, Phys. Rev. Lett. **85**, 5360 (2000).

[21] C. Donati, F. Sciortino, and P. Tartaglia, Role of Unstable Directions in the Equilibrium and Aging Dynamics of Supercooled Liquids, Phys. Rev. Lett. **85**, 1464 (2000).

[22] B. Doliwa and A. Heuer, What Does the Potential Energy Landscape Tell Us about the Dynamics of Supercooled Liquids and Glasses? Phys. Rev. Lett. **91**, 235501 (2003).

[23] L. Berthier, Time and length scales in supercooled liquids, Phys. Rev. E **69**, 020201 (2004).

[24] S. Whitelam, L. Berthier, and J. P. Garrahan, Dynamic Criticality in Glass-Forming Liquids, Phys. Rev. Lett. **92**, 185705 (2004).

[25] E. Flenner and G. Szamel, Anisotropic spatially heterogeneous dynamics in a model glass-forming binary mixture, J. Phys. Condens. Matter **19**, 205125 (2007).

[26] L. Berthier and G. Biroli, Theoretical perspective on the glass transition and amorphous materials, Rev. Mod. Phys. **83**, 587 (2011).

[27] M. D. Ediger, Spatially heterogeneous dynamics in supercooled liquids, Ann. Rev. Phys. Chem. **51**, 99 (2000).

[28] W. Kob and H. C. Andersen, Kinetic lattice-gas model of cage effects in high-density liquids and a test of mode-coupling theory of the ideal-glass transition, Phys. Rev. E **48**, 4364 (1993).

[29] S. Plimpton, Fast parallel algorithms for short-range molecular dynamics, J. Comp. Phys. **117**, 1 (1995).

[30] A. R. Yavari, A. Le Moulec, A. Inoue, N. Nishiyama, N. Lupu, E. Matsubara, W. J. Botta, G. Vaughan, M. Di Michiel, and A. Kvick, Excess free volume in metallic glasses measured by X-ray diffraction, Acta Mater. **53**, 1611 (2005).

[31] G. Dlubek, A. P. Clarke, H. M. Fretwell, S. B. Dugdale, and M. A. Alam, Positron lifetime studies of free volume hole size distribution in glassy polycarbonate and polystyrene, Phys. Stat. Sol. (A) **157**, 351 (1996).

[32] S. Sastry, D. S. Corti, P. G. Debenedetti, and F. H. Stillinger, Statistical geometry of particle packings. I. Algorithm for exact

determination of connectivity, volume, and surface areas of void space in monodisperse and polydisperse sphere packings, Phys. Rev. E **56**, 5524 (1997).

[33] Z. Shi, P. G. Debenedetti, F. H. Stillinger, and P. Ginart, Structure, dynamics, and thermodynamics of a family of potentials with tunable softness, J. Chem. Phys. **135**, 084513 (2011).

[34] R. L. Martin, B. Smit, and M. Haranczyk, Addressing challenges of identifying geometrically diverse sets of crystalline porous materials, J. Chem. Inf. Model. **52**, 308 (2012).

[35] T. F. Willems, C. H. Rycroft, M. Kazi, J. C. Meza, and M. Haranczyk, Algorithms and tools for high-throughput geometry-based analysis of crystalline porous materials, Micropor. Mesopor. Mater. **149**, 134 (2012).

[36] T. Nakayama, K. Yakubo, and R. L. Orbach, Dynamical properties of fractal networks: Scaling, numerical simulations, and physical realizations, Rev. Mod. Phys. **66**, 381 (1994).

[37] G. T. Barkema, J. F. Marko, and J. de Boer, Transient and asymptotic domain growth in the 3D Ising model with conserved spin, Europhys. Lett. **26**, 653 (1994).

[38] T. M. Rogers, K. R. Elder, and R. C. Desai, Numerical study of the late stages of spinodal decomposition, Phys. Rev. B **37**, 9638 (1988); R. Toral, A. Chakrabarti, and J. D. Gunton, Effect of the morphology of patterns on the scaling functions: Off-critical quenches, *ibid.* **39**, 901 (1989); A. Shinozaki and Y. Oono, Asymptotic Form Factor for Spinodal Decomposition in Three-Space, Phys. Rev. Lett. **66**, 173 (1991).

[39] S. van Gemmert, G. T. Barkema, and S. Puri, Phase separation driven by surface diffusion: A Monte Carlo study, Phys. Rev. E **72**, 046131 (2005).

[40] M. J. Nuevo, J. J. Morales, and D. M. Heyes, Temperature and density dependence of the self-diffusion coefficient and Mori coefficients of Lennard-Jones fluids by molecular dynamics simulation, Phys. Rev. E **55**, 4217 (1997).